

## Research Paper

# Temperature-controlled, phase-transition ultrasound imaging-guided photothermal-chemotherapy triggered by NIR light

Wei Li<sup>#1</sup>, Wanqing Hou<sup>#1</sup>, Xiaomeng Guo<sup>1</sup>, Lihua Luo<sup>1</sup>, Qingpo Li<sup>1</sup>, Chunqi Zhu<sup>1</sup>, Jie Yang<sup>1</sup>, Jiang Zhu<sup>2</sup>, Yongzhong Du<sup>1</sup>, Jian You<sup>1</sup>✉

1. College of Pharmaceutical Sciences, Zhejiang University, Yuhangtang Road 866, Hangzhou 310058, People's Republic of China
2. Sir Run Run Shaw Hospital, Zhejiang University School of Medicine, Hangzhou 310016, People's Republic of China

<sup>#</sup> These authors contributed equally to this work.

✉ Corresponding author: Jian You, College of Pharmaceutical Sciences, Zhejiang University, Yuhangtang Road 866, Hangzhou 310058, People's Republic of China; Tel: 086-571-88981651; Fax: 086-571-88208439; E-mail: youjiandoc@zju.edu.cn

© Ivyspring International Publisher. This is an open access article distributed under the terms of the Creative Commons Attribution (CC BY-NC) license (<https://creativecommons.org/licenses/by-nc/4.0/>). See <http://ivyspring.com/terms> for full terms and conditions.

Received: 2017.11.16; Accepted: 2018.03.15; Published: 2018.04.30

## Abstract

Recently, nano-sized ultrasound contrast agents encapsulating drugs for cancer diagnosis and therapy have attracted much attention. However, the ultrasound signal of these agents is too weak to obtain an ideal ultrasound imaging effect. Furthermore, conventional ultrasound contrast agents with strong echo signal are not suitable for drug delivery against cancer because of their large size. To circumvent this problem, phase-transition ultrasound contrast agents are believed to be an excellent choice.

**Methods:** Liposomes co-encapsulating doxorubicin (DOX), hollow gold nanospheres (HAuNS), and perfluorocarbon (PFC) were synthesized by film dispersion method. The morphology, particle size, and stability of these liposomes (DHPL) were investigated. The photothermal effect, drug release, particle size change, cytotoxicity, and ultrasound imaging were studied by using the near infrared (NIR) light. Furthermore, tumor accumulation of DHPL was observed by *in vivo* fluorescence imaging and the antitumor effect was verified in a 4T1 tumor model.

**Results:** The nanosystem displayed a homogeneous size distribution (~200 nm) and an efficient light-to-heat conversion effect under 808 nm NIR laser irradiation. The nanometer size enabled considerable accumulation of DHPL in the tumor sites. The localized hyperthermia resulting from the photothermal effect of HAuNS could trigger the size transformation of DHPL followed by significant DOX release. Due to the gasification of PFC, a remarkably enhanced ultrasound signal was detected. DHPL also exhibited a prominent photothermally reinforced chemotherapeutic effect under the control of NIR light both *in vitro* and *in vivo*. Importantly, no systemic toxicity was observed by DHPL treatment.

**Conclusion:** In this study, we fabricated multi-functional perfluorocarbon liposomes for ultrasound imaging-guided photothermal chemotherapy which have the potential to serve as a prospective cancer treatment approach.

Key words: Hollow gold nanospheres; Perfluorocarbon; NIR light; Ultrasound imaging; Photothermal-chemotherapy

## Introduction

As a noninvasive diagnostic technique, ultrasound imaging has been successfully applied for the clinical diagnosis of various diseases due to its high security, low cost, and good patient compliance [1]. To improve the contrast and spatial resolution of

gray-scale imaging, ultrasound microbubble contrast agents such as SonoVue<sup>®</sup> are employed in the clinic [2, 3]. Taking advantage of the enlarged reflection of the sound wave to gas compared with liquid (about 1000 times) and the non-linear acoustic effect of

microbubbles, the ultrasonic echo could be enhanced to achieve disease diagnosis. The size of microbubble contrast agents is usually in the range of 1-10  $\mu\text{m}$ , enabling them to reach the lesion sites for ultrasound imaging [4, 5]. However, because of the rapid elimination from the body, neither the traditional microbubble contrast agents, nor their co-delivery system with therapeutic drugs can maintain sufficient retention time at the tumor site [6]. Also, the microbubbles only remain in the blood vessels rather than penetrate into the tumor tissue, restricting tumor detection, ultrasound imaging, and the delivery of therapeutic agents to tumor sites [4, 7, 8]. Therefore, nano-sized ultrasound contrast agents, such as liquid fluothane nanoparticles and some other nanocarriers free from gas, have been widely studied in recent decades to obtain a deep tissue distribution [5, 9-11]. Nevertheless, unlike the microbubbles with high sensitivity for ultrasound detection, these contrast agents exhibit a relatively lower echogenicity resulting from the insufficient accumulation in the tumor sites [12, 13]. Thus, the contradiction between the tissue distribution and the echogenicity for ultrasound contrast agents has become a serious problem that needs to be urgently resolved [14].

Thermal therapy could render cancer cells more sensitive to radio- or chemo-therapy, which are considered as ideal adjuvant methods for cancer treatment [15]. Thermotherapy can cure cancers since cells cannot survive hyperthermia despite complicated DNA mutations. The key factor in this technique is the delivery of heat specifically to tumor cells avoiding the normal cells. Photothermal therapy (PTT), which employs light-absorbers such as metallic nanocarriers to convert light from specific wavelength to heat, provides a significantly increased specificity of heat delivery into tumors. Therefore, PTT is becoming a promising cancer therapy approach [16, 17]. Hollow gold nanospheres (HAuNS) with small particle size (30-50 nm) and excellent light-to-heat conversion efficiency, have been used as a photothermal therapy agent for a variety of cancers [18]. However, the nanospheres only reach the regions with abundant blood vessels, resulting in an inhomogeneous heat distribution and failure of photothermal ablation to eliminate tumor cells from poorly vascularized regions of the tumor [19]. The surviving cancer cells then become the underlying reason of tumor recurrence [20]. To address this problem, the combination of photothermal therapy and chemotherapy is the method of choice for subjecting the malignant tumors to “dual-strike” [21].

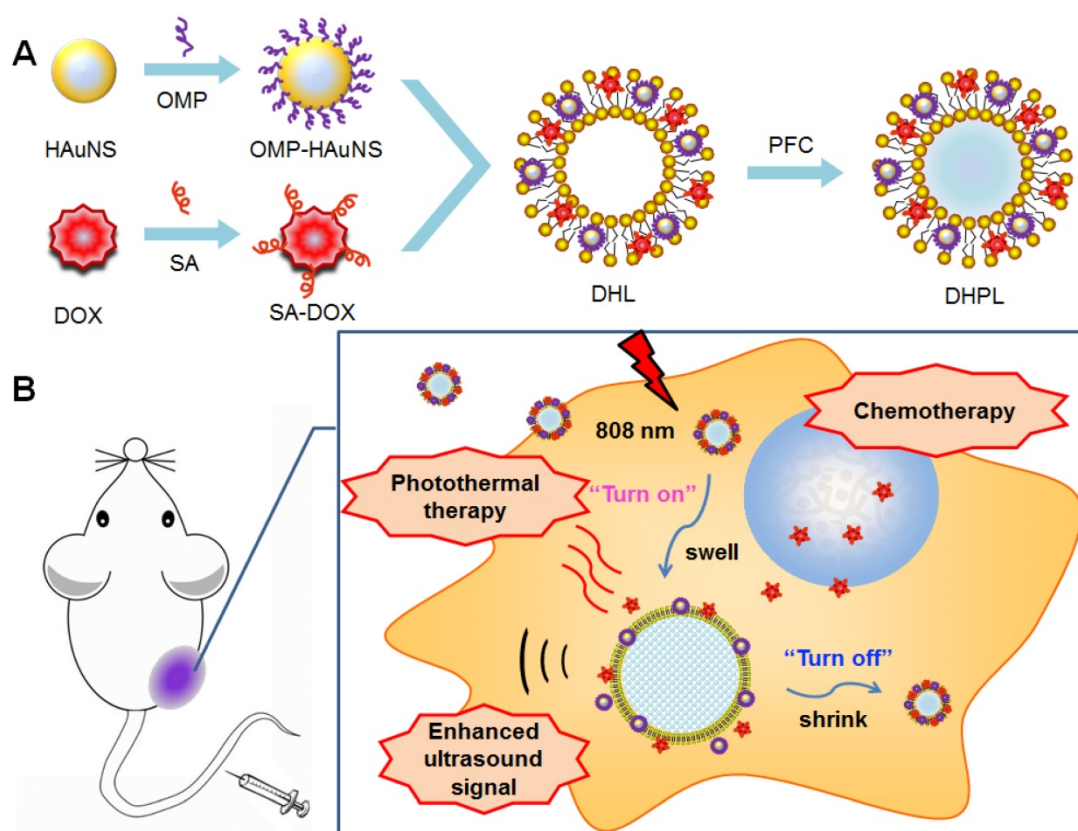
In this study, we report a phase-transition ultrasound contrast agent with combined capability of photothermal/chemo cancer therapy controlled by

NIR (808 nm) irradiation. This nanosystem (DHPL) was constructed by co-encapsulating perfluorocarbon (PFC) with low boiling point (perfluorohexane, PFH, 59 °C; or perfluoropentane, PFP, 29 °C), hydrophobic modified HAuNS (octadecyl 3-Mercaptopionate conjugated HAuNS, OMP-HAuNS) and DOX (stearic acid conjugated DOX, SA-DOX) in the liposomes (**Scheme 1A**). The heat generated by HAuNS under NIR laser irradiation was able to trigger DOX release as well as the gasification of liquid PFC. Thus, a significant particle swelling was achieved, which dramatically enhanced the ultrasound signal of DHPL (“turn-on”). After the laser exposure, DHPL shrunk back to the normal size along with the decreased temperature (“turn-off”). An extraordinary anti-tumor effect was observed due to the photothermally reinforced chemotherapeutic efficacy (**Scheme 1B**). Our results demonstrate that the ultrasound imaging-guided nanosystem described here is highly controllable and biocompatible and has the potential to be a promising approach for cancer therapy.

## Methods

### Materials

Sodium citrate (>99 %), sodium borohydride (99 %), cobalt chloride hexahydrate (99.99 %), chloroauric acid trihydrate (American Chemical Society reagent grade), 3-(4,5-dimethylthiazol-2-yl)-2,5-diphenyltetrazolium bromide (MTT reagent) and Hoechst 33324 were purchased from Sigma-Aldrich Inc. (St Louis, MO, USA). 1-Ethyl-3-(3-dimethylaminopropyl) carbodiimide (EDC) was acquired from Thermo Fisher Scientific (Waltham, MA, USA). Octadecyl 3-Mercaptopionate (OMP) was supplied by Tokyo Chemical Industry Co. (Tokyo, Japan). Doxorubicin hydrochloride (DOX•HCl) was purchased from Hisun Pharmaceutical Co., Ltd. (Zhejiang, China). 1,1'-Diiodo-3,3',3'-Tetramethylindotricarbocyanine Iodide (DiR) was obtained from Invitrogen Co. (Carlsbad, CA, USA). Stearic acid (SA) was supplied by Aladdin Co., Ltd. (Shanghai, China). Soya bean lecithin (S100), 1,2-distearoyl-sn-glycero-3-phosphoethanolamine-N-[methoxy(polyethylene-glycol)-2000] (DSPE-PEG<sub>2000</sub>) were obtained from lipid Co. (Ludwigshafen, Germany). Sulphur Hexafluoride Microbubbles for Injection (SonoVue<sup>®</sup>) was supplied by Bracco Imaging B.V. Co. (Switzerland). RPMI-1640 medium (RPMI), Dulbecco's Modified Eagle Medium (DMEM), trypsin, fetal bovine serum (FBS) and penicillin/streptomycin (100 U/mL) were purchased from Ji Nuo Biotechnology Co., Ltd. (Zhejiang, China). The chemicals and solvents were of analytical grade and were used as received.



**Scheme 1.** The construction and the antitumor mechanism of DHPL. (A) The construction procedure of DHPL. (B) The antitumor and ultrasound imaging mechanism of DHPL.

### Cell culture and animal model

MCF-7 (human breast carcinoma), 4T1 (mice breast cancer) and HEK293 (human embryonic kidney) cell lines were obtained from Institute of Biochemistry and Cell Biology (Shanghai, China). Cells were cultured in RPMI 1640 culture medium (MCF-7) or Dulbecco's Modified Eagle Medium (4T1 and HEK293) containing 10 % fetal bovine serum (Life Technologies, Inc., Carlsbad, CA) at 37 °C in a humidified atmosphere with 5 % CO<sub>2</sub>.

All the animal studies were performed as the Institutional Animal Care and Use Committee approved methods. Male balb/c mice (6-8 weeks old, ~20 g) were inoculated subcutaneously at the breast fat pad with 2×10<sup>6</sup> 4T1 cells and allowed to grow to solid tumors.

### Synthesis and hydrophobization of hollow gold nanoparticles (HAuNS)

The HAuNS were synthesized using our previously reported procedures [18, 22]. In brief, cobalt nanoparticles were obtained by mixing 2.8 mL sodium citrate (0.1 M), 1.0 mL cobalt chloride (0.4 M) and 4 mL sodium borohydride (1 M) in deionized water. Subsequently, chloroauric acid trihydrate was added and the Au ions were reduced onto the surface

of the cobalt nanoparticles. HAuNS (4 mg) were obtained by oxidizing the cobalt nanoparticles to cobalt oxide under continuous stirring in the presence of air. Further purification and compression were realized by centrifuging the solution at 5,600 ×g for 10 min. The precipitate was dissolved in DMF, mixed with 50 mg 3-mercaptopropionic acid octadecyl ester (OMP), and stirred overnight under the presence of argon. The product was further centrifuged to obtain OMP-HAuNS and dispersed in chloroform. The spectrum of HAuNS was acquired with UV-vis spectrometer (Cary 60, Agilent Co., USA) and the morphology of HAuNS and OMP-HAuNS was observed by transmission electron microscope (TEM, JEM-100S, JEOL, Japan). The nanoparticle size was measured by dynamic light scattering (DLS) with a Zetasizer (ZS90, Malvern Co., UK).

### Synthesis of stearic acid modified DOX (SA-DOX)

DOX was modified with hydrophobic stearic acid for further use. Briefly, 5.4 mg stearic acid were mixed with EDC (SA: EDC=1:10, mol/mol) in 4 mL HCl (pH=2) acidified DMSO at 60 °C and stirred for 30 min. After the pH value of the reaction solution was adjusted to ~8 by triethylamine, 10 mg DOX·HCl were added, followed by a moderate stir for another

24 h. The resulted solution was dialyzed (3.5 kDa) with purified water for 48 h. SA-DOX powder was collected after lyophilization (Freezone, Labconco CO., England). The chemical structure of the obtained SA-DOX was identified by  $^1\text{H}$  NMR.

### Preparation of DOX and HAuNS loaded PFC liposomes (DHPL)

A lipid film hydration-extrusion method was employed to prepare DHPL. Specifically, 15 mg S100, 5.58 mg DSPE-PEG<sub>2000</sub>, 2 mg SA-DOX and 0.4 mg OMP-HAuNS were dissolved in 5 mL chloroform, evaporated to form a thin lipid film, which was then hydrated and sonicated to obtain homogeneous liposomes (DOX&HAuNS- loaded liposomes, DHL). Subsequently, DOX and HAuNS loaded PFC liposomes (DHPL) were prepared by mixing 60  $\mu\text{L}$  PFC with DHL and sonicated under ice bath. DOX-loaded PFC liposomes (DPL) and HAuNS-loaded PFC liposomes (HPL) were also prepared by using the same method. The obtained liposomes were purified by dialysis and chromatography using a Sephadex G-50 column and eluted with PBS buffer (pH=7.4) in the absence of light. The nanoparticle size of DHPL at 4 °C was measured by a Zetasizer and the encapsulation of OMP-HAuNS was observed by TEM. The encapsulation efficiency (EE) of DOX in DHPL was estimated using a fluorescence spectrophotometer (F-2500, HITACHI Co., Japan). Briefly, the purified DHPL were demulsified by ethanol followed by the water-bath sonication for 10 min. Then, the fluorescence of DOX (Ex: 505 nm, Em: 565 nm) was measured and compared with that of initial dosage. The EE of DOX in DHPL was calculated according to the formula  $F_i/F_t \times 100\%$ , where  $F_i$  indicates the amount of DOX encapsulated in the liposomes and  $F_t$  indicates the total dosage of DOX.

### NIR-mediated temperature elevation *in vitro*

0.5 mL DHPL solutions containing 20, 40 or 200  $\mu\text{g}/\text{mL}$  HAuNS were exposed to continuous 808 nm light irradiation respectively at the laser power of 1  $\text{W}/\text{cm}^2$  or 2  $\text{W}/\text{cm}^2$  (Diomed 15 plus, Cambridge, UK) for 10 min. The temperature of each sample was detected by a temperature probe every 20 s. PBS with an equal volume was employed as a control.

### NIR-mediated drug release *in vitro*

0.5 mL purified DHPL or DPL were diluted in 4.5 mL PBS buffer (pH=7.4) containing 10 % (v/v) DMSO and vibrated (56 rcf) at 37 °C. The samples were centrifuged (5,600  $\times g$ , 10 min) after 0, 0.5, 1, 2, 4, 6, and 8 h. Subsequently, 4.5 mL supernatant was used to detect DOX fluorescence, and the residual 0.5 mL solution was treated with 808 nm laser irradiation

at 2 and 6 h (2  $\text{W}/\text{cm}^2$ , 3 min) to investigate the NIR-mediated SA-DOX release. Next, 4.5 mL fresh release medium was added to continue the release study. The concentration of DOX at each time point was determined using a standard curve and the cumulative release percentage was calculated.

### Temperature-induced size change

We examined the possibility that different kinds of PFC might play important roles in the size change of DHPL depending on the gasification of PFC. Therefore, perfluorohexane (PFH, boiling point 59 °C) or perfluoropentane (PFP, boiling point 29 °C) were employed to prepare two different DHPLs (0.5  $\text{mg}/\text{mL}$  HAuNS, 30  $\mu\text{L}/\text{mL}$  PFC; named DHPL-59 or DHPL-29, respectively), which were diluted 50 times with PBS (pH=7.4). The particle size of each sample was determined by a Zetasizer under various temperatures. To simulate the higher viscosity of blood and the extracellular fluid compared with PBS, 0.1 % or 0.01 % hydroxy-propyl methyl cellulose (HPMC) solutions were employed to dilute the two DHPLs. The change in particle size was investigated at 4, 25, 37, 42, 62, and 82 °C. Also, to determine whether DHPL could undergo the temperature-induced reversible conversion of the particle size, the size change of DHPL in PBS or HPMC solution was examined after repeated heating-cooling cycles for three times at 37, 42, 62, and 92° C. Furthermore, to observe the size change of DHPL directly, DHPL was added to a cell plate and the generation of microbubbles was observed following laser treatment (2  $\text{W}/\text{cm}^2$ , 2 min) using a fluorescence microscope.

### Ultrasound imaging *in vitro*

First, a hole model (pore size: 1 cm) was made using 1 % Sephadex gel as the imaging matrix. 0.2 mL DHPL-59 (0.5  $\text{mg}/\text{mL}$  HAuNS) or DPL@HAuNS (physical mixture of DPL and HAuNS, 0.5  $\text{mg}/\text{mL}$  HAuNS) was added into the hole, followed by different laser treatments (1  $\text{W}/\text{cm}^2$  or 2  $\text{W}/\text{cm}^2$ ). The ultrasound signal of the samples was recorded using an ultrasound diagnostic apparatus (IU22, Philips, NL). PBS was used as negative control. The signal intensity was analyzed by "Image J" software.

### Cellular internalization

MCF-7 or 4T1 cells were seeded on 20 mm glass coverslips overnight and then incubated with DHPL, DPL, or SA-DOX respectively at the concentration of 1  $\mu\text{M}$  DOX for 2, 6 and 12 h. Next, the cells were rinsed with PBS for three times and the cell nuclei were stained with Hoechst 33342, followed by the observation of DOX fluorescence using a confocal microscopy (A1R, Nikon, Japan).

### Cytotoxicity *in vitro*

MCF-7, 4T1 or HEK293 cells were seeded on a 96-well plate to grow and then incubated with DOX•HCl, SA-DOX, DPL, HPL, or DHPL respectively at different DOX or HAuNS concentrations (0.01, 0.1, 1, 10  $\mu$ M, n=5). After 12 h incubation, the drug medium in each well was replaced by fresh culture medium. Subsequently, cells in DPL, HPL, or DHPL group were exposed to 808 nm laser illumination (1 W/cm<sup>2</sup>, 3 min). Cells without laser treatment were used as controls. After another 12 h, the standard MTT assay was performed to estimate the cytotoxicity of the drugs. The results were expressed as cell viability compared with the control group.

### Ultrasound imaging *in vivo*

When the 4T1 tumor volume reached about 300 mm<sup>3</sup>, 0.2 mL DHPL-29 (30  $\mu$ L/mL PFP, 0.5 mg/mL HAuNS) was intravenously injected into the mice body. After 24 or 48 h, tumors were treated with laser irradiation (2 W/cm<sup>2</sup>) and the ultrasound signal was detected using an ultrasound diagnostic apparatus (IU22, Philips, NL) before and after the laser exposure (frequency: 1.9 M Hz). Mice with intravenous injection of SonoVue<sup>®</sup> were employed as positive control.

### Biodistribution of DHPL in 4T1 tumor-bearing balb/c mice

DHPL was first labeled with DiR. Briefly, 15 mg S100, 5.58 mg DSPE-PEG<sub>2000</sub>, 2 mg SA-DOX, 0.4 mg OMP-HAuNS and 0.1 mg DiR were dissolved in 5 mL chloroform and evaporated to form a thin lipid film. The film was then hydrated and sonicated to obtain DiR-labeled DHL. Then, DiR-labeled DHPL were prepared by adding 60  $\mu$ L PFH and sonicating under ice bath.

When 4T1 tumor volume reached about 300 mm<sup>3</sup>, the mice were injected with 0.2 mL DiR-labeled DHPL (DOX: 0.5 mg/mL) through tail vein and observed by an *in vivo* imaging system (Maestro EX, CRI Inc., Woburn, MA) at 24, 48, 72 h post-injection. After the mice were sacrificed, the major organs (heart, liver, spleen, lung, kidney) were excised for further imaging analysis. A 5 % injection dose solution was used as a control and the biodistribution of DHPL in each organ was expressed as %ID/g (percentage of injection dose per gram).

### Tumor growth inhibition *in vivo*

When the tumors reached about ~60 mm<sup>3</sup> in size, mice bearing 4T1 tumors were randomly divided into five groups and intravenously injected with 0.2 mL PBS (n=7), DOX•HCl (3.55 mg/kg DOX, n=7), DPL

(3.55 mg/kg DOX, n=7), HPL (5 mg/kg HAuNS, n=7), or DHPL (3.55 mg/kg DOX, 5 mg/kg HAuNS, n=7) on days 0, 2, and 4 (once per day). The tumors in group HPL and DHPL were exposed to laser illumination on days 1, 3, and 5 (1 W/cm<sup>2</sup>, 3 min, once per day). The tumor volume was measured by a vernier caliper every two days and calculated using the formula:  $V \text{ (mm}^3\text{)} = LWH \times \pi / 6$ , where L, W, and H indicate length, width, height, respectively, and  $\pi$  denotes PI. The body weight was also monitored throughout the whole treatment process. The mice were all sacrificed at day 22 and the tumors as well as major organs (heart, liver, spleen, lung, kidney) were collected for H&E, Tunnel and Ki-67 staining to estimate anti-tumor effects as well as therapeutic safety.

### Statistical analysis

Pairs of samples were compared using Student's *t* test by one-way analysis of variance (ANOVA) test.  $P < 0.05$  was regarded as statistical significance and  $P^{**} < 0.01$  was regarded as markedly statistical significance.

## Results

### Characterization of DHPL

We identified the chemical structure of SA-DOX by <sup>1</sup>H NMR. As shown in **Figure S1**, free SA exhibited the characteristic peak of the carboxyl group at about 12 ppm which disappeared after conjugating with DOX. Besides, a peak of acyl group was observed in SA-DOX, indicating the successful synthesis of SA-DOX.

HAuNS showed an obvious absorption in the NIR region with a characteristic peak at 808 nm due to the surface plasmon resonance (SPR) (**Figure S2A**), while DHPL exhibited the characteristic absorption peaks of both HAuNS and DOX at 808 nm and 505 nm, respectively (**Figure 1A**). The average size of HAuNS was  $35.8 \pm 1.2$  nm (polydispersity index, PDI:  $0.007 \pm 0.004$ ), indicating that HAuNS could be used as an excellent photothermal conversion material with homogeneous size distribution. As displayed in **Figure 1B**, HAuNS exhibited a hollow structure inside a 5-10 nm spherical shell. The surface of OMP-HAuNS was surrounded by a thin macromolecular layer, which was indicative of the successful modification of OMP. The particle size of DHPL was  $196.6 \pm 17.6$  nm at 4 °C with a PDI of  $0.165 \pm 0.044$ . HAuNS were encapsulated inside the lipid membrane of DHPL (**Figure 1B**). Co-encapsulating OMP-HAuNS and SA-DOX in the liposomes led to slight fluorescence quenching of DOX according to the fluorescence spectra (**Figure S2B**). After repeated purification for removing the unstable absorption on

the surface of the liposomes, the entrapment efficiency (EE) of SA-DOX in DHPL was verified to be  $49.27 \pm 1.60 \%$ . The drug loading content (DL) was  $4.4 \pm 0.27 \%$ , which could meet the requirements of the subsequent experiments.

The stability of DHPL was also investigated by recording the change of size and zeta potential after storing the samples (in water or serum) at room temperature for one week. As presented in **Figure S3A-B**, DHPL exhibited negative surface electricity of  $-24.8 \pm 0.36$  and  $-18.6 \pm 0.21$  mV in water and serum, respectively. Both the particle size and zeta potential were stable for seven days, demonstrating the excellent stability of DHPL in water or serum.

### Photothermal efficiency and drug release behavior of DHPL *in vitro*

The temperature elevation of the DHPL-59 solution containing different concentrations of HAuNS (20, 40 or 200  $\mu\text{g}/\text{mL}$ ) was investigated under NIR light irradiation (1  $\text{W}/\text{cm}^2$  or 2  $\text{W}/\text{cm}^2$ ). The results are displayed in **Figure 1C** and **Figure S4**. Laser exposure caused a significant temperature rise of DHPL within 10 min while PBS exhibited only a slight temperature change under the same laser conditions. Furthermore, the light-to-heat conversion efficiency was closely related to the concentration of HAuNS and the laser power density. DHPL-59 containing 200  $\mu\text{g}/\text{mL}$  HAuNS reached  $\sim 100^\circ\text{C}$  after 5 min illumination (2  $\text{W}/\text{cm}^2$ ), demonstrating the extraordinary photothermal efficiency mediated by

NIR light. The photothermal conversion efficiency of DHPL-59 was about 47.4 % as calculated by a previously reported method [23].

The NIR-triggered DOX release from DHL or DHPL-59 was also investigated. As shown in **Figure 1D**, DHPL-59 exhibited the highest release profile following two treatments with the laser (2  $\text{W}/\text{cm}^2$ , 3 min). Almost all DOX (95.57 %) was released after 8 h while DPL only released 49.21 % DOX under the same conditions. As controls, DHPL-59 or DPL with no laser exposure did not show an enhanced DOX release behavior in 8 h (57.46 % and 52.11 %, respectively). The increased drug release might be attributed to the photothermal effect of HAuNS mediated by NIR light.

### The temperature-induced size change of DHPL

Two kinds of DHPLs (DHPL-59, boiling point  $59^\circ\text{C}$ ; DHPL-29, boiling point  $29^\circ\text{C}$ ) were synthesized to investigate the gasification-related size change mediated by NIR light. The temperature rise was controlled by Zetasizer to simulate the HAuNS induced hyperthermia. As displayed in **Figure 2A**, the size increase of DHPL-29 was significantly greater than that of DHPL-59 when the temperature was elevated. In HPMC, which had a higher viscosity than PBS, the size changes of DHPL-59 and DHPL-29 were comparable with those in PBS. It also appeared that increase in medium viscosity could hinder the growth rate of the particle size (**Figure 2B**).

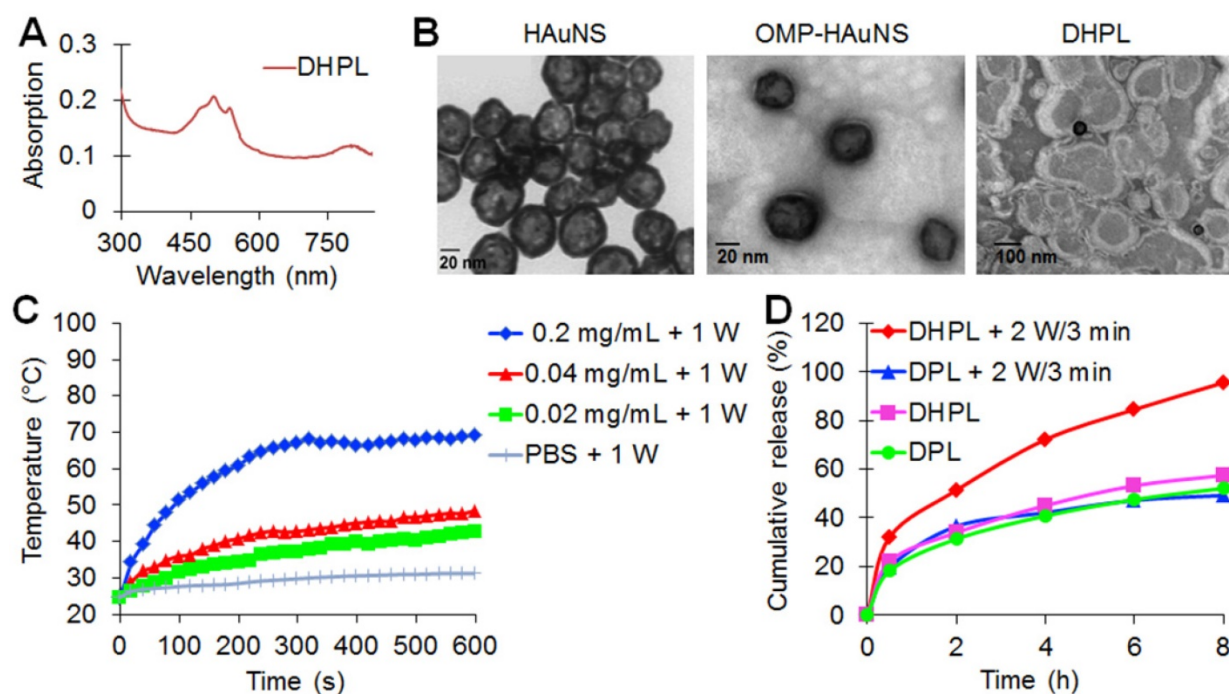


**Figure 1. Characterization of DHPL. (A)** UV-vis absorption spectrum of DHPL. **(B)** Representative transmission electron microscope (TEM) images of HAuNS, OMP-HAuNS and DHPL, respectively. **(C)** The temperature elevation curves of DHPL-59 containing various HAuNS concentrations or PBS under NIR laser (1  $\text{W}/\text{cm}^2$ ). **(D)** SA-DOX release from DPL or DHPL-59 with (2  $\text{W}/\text{cm}^2$  for 3 min, at 2 and 6 h) or without NIR laser.

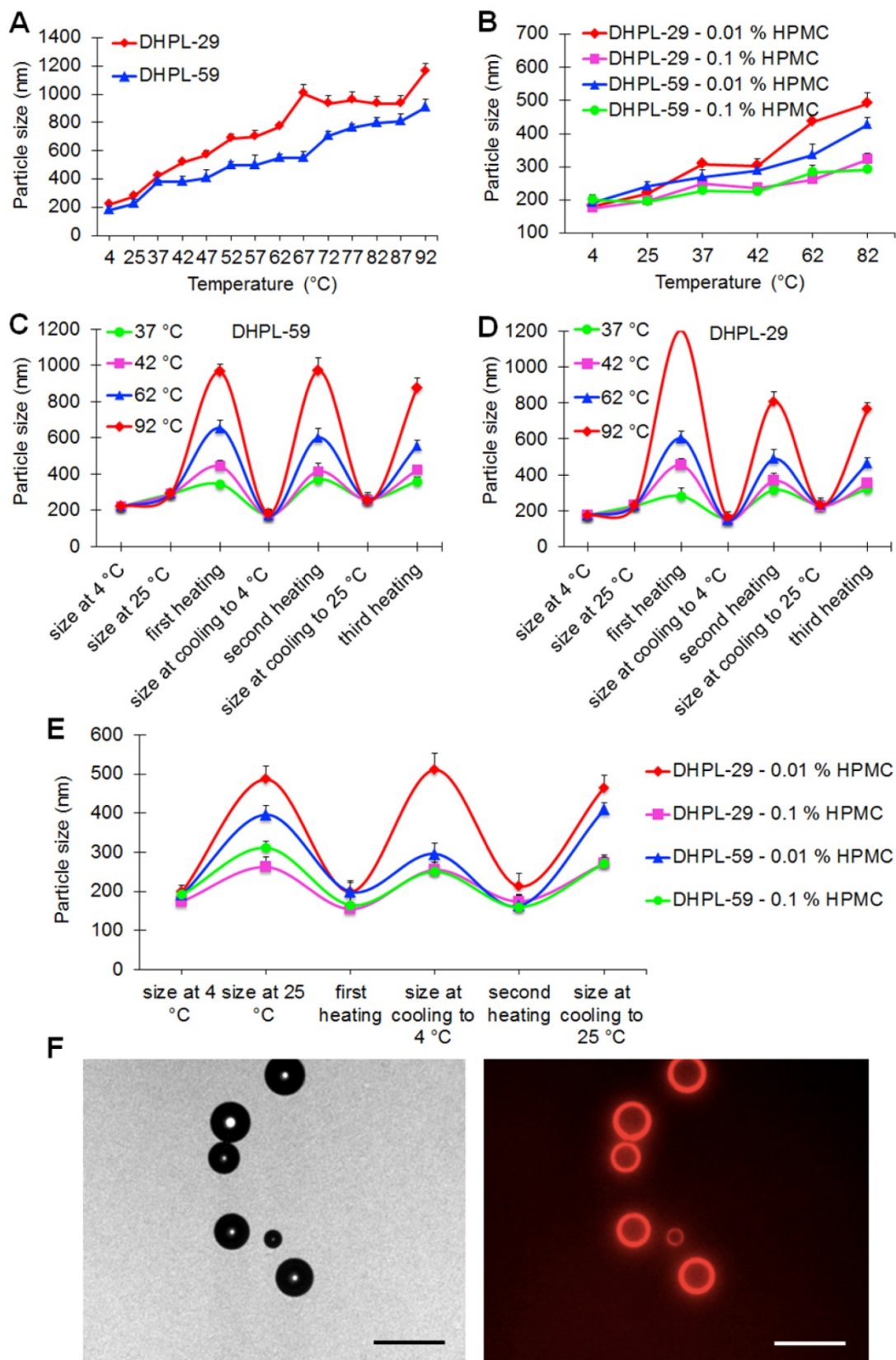


**Figure 2. Temperature-induced size change of DHPL.** (A) Particle size changes of DHPL-29 and DHPL-59 in PBS at various temperatures (n=3). (B) Particle size changes of DHPL-29 and DHPL-59 in HPMC solutions at various temperatures (n=3). (C) Particle size changes of DHPL-59 in PBS during three heating-cooling cycles at four different temperatures (n=3). (D) Particle size changes of DHPL-29 in PBS during three heating-cooling cycles at four different temperatures (n=3). (E) The particle size changes of DHPL-59 and DHPL-29 in HPMC solutions during three heating-cooling cycles at 82 °C (n=3). (F) The photomicrographs (left) and fluorescence photomicrographs (right) of the microbubbles produced by DHPL-59 after NIR light irradiation (2 W/cm<sup>2</sup>, 2 min). Scale bars, 20 μm.

To verify the size conversion ability of DHPL, the size change of DHPL solutions diluted with PBS or HPMC was further determined under three heating-cooling cycles. The results demonstrated that the heating caused DHPL to swell and the subsequent cooling induced the shrinkage of particles (**Figure 2C-D**). The size change tendency of DHPL-59 was similar to that of DHPL-29, although there was less enlargement with the temperature rise. For example, the size of DHPL-29 reached about 1300 nm (**Figure 2D**) while that of DHPL-59 only increased to about 1000 nm (**Figure 2C**) at 92 °C. Similar phenomena were observed when DHPL was suspended in HPMC solutions with a decreased size enlargement compared to that in PBS (**Figure 2E**). These results indicated that the particle size of DHPL was temperature-dependent and was able to be swell-shrink during the heating and cooling cycle. For

a better stability, DHPL-59 was employed in the subsequent experiments (named hereafter DHPL).

To investigate the microbubble generation, DHPL solution was illuminated by NIR light (2 W/cm<sup>2</sup>, 2 min) and then observed by a fluorescence microscope (Nikon, Japan). A few microbubbles were found in the drug solution with DOX fluorescence around the surface (**Figure 2F**), indicating that DHPL could be a potential ultrasound imaging agent mediated by NIR light.

### Ultrasound imaging *in vitro*

A 1 % Sephadex gel with an 808 nm laser fiber inserted was used as the imaging matrix of the hole model (**Figure 3A**). The ultrasound imaging of both HAuNS@DPL (physical mixture of HAuNS and DPL) and DHPL showed an enhanced signal within 5 min of NIR light irradiation (1 W/cm<sup>2</sup>) (**Figure 3B-C**).

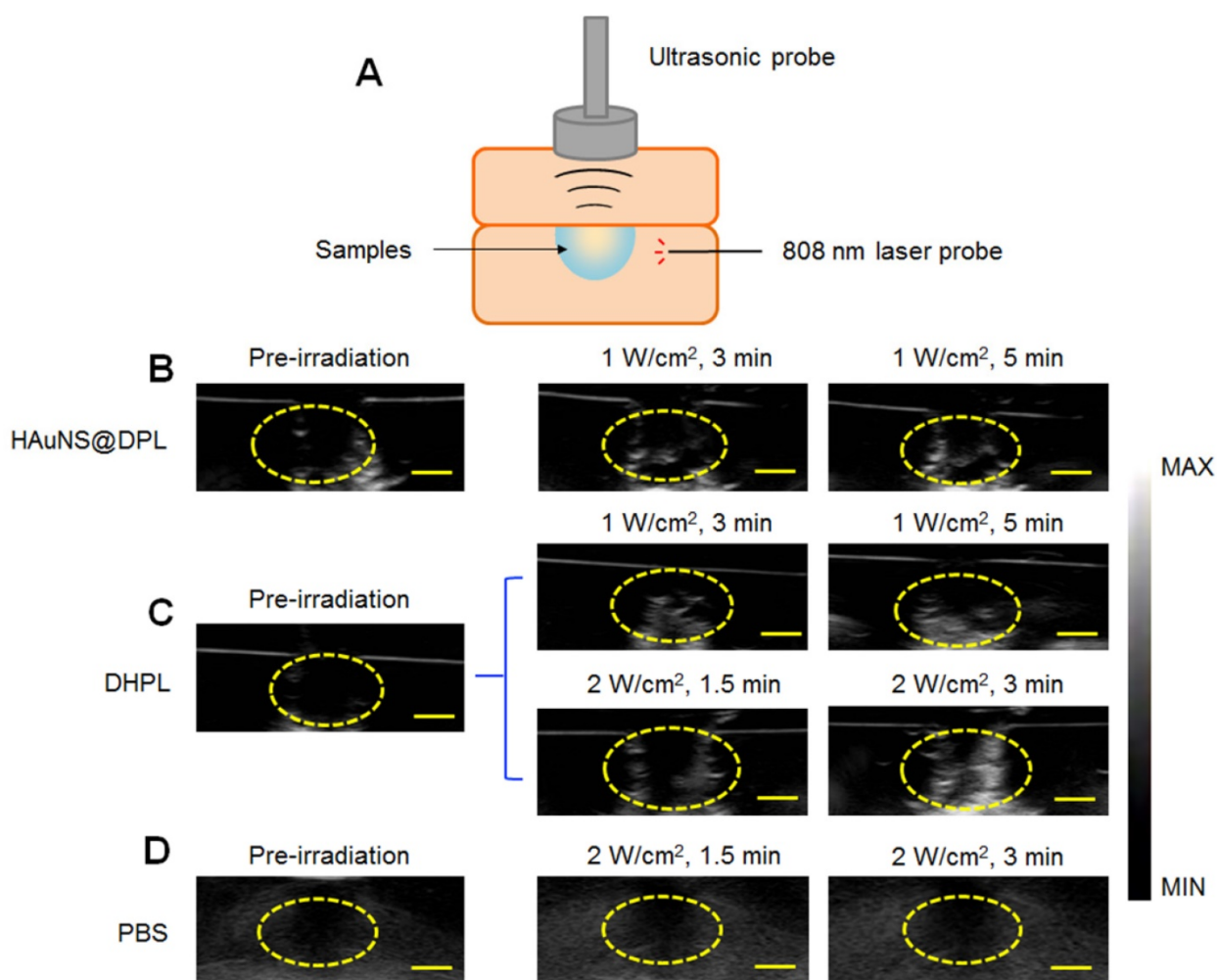


**Figure 3. Ultrasound imaging *in vitro*.** (A) A hole model (pore size: 1 cm) made by 1 % Sephadex gel as the imaging matrix with an 808 nm laser fiber inserted. (B) Representative ultrasound images of HAuNS@DPL (0.5 mg/mL HAuNS) under NIR light irradiation (1 W/cm<sup>2</sup>). (C) Representative ultrasound images of DHPL-59 (0.5 mg/mL HAuNS) under NIR light irradiation (1 W/cm<sup>2</sup> or 2 W/cm<sup>2</sup>). (D) Representative ultrasound images of PBS as a negative control after NIR light irradiation (2 W/cm<sup>2</sup>). Yellow circles: region of interest (ROI). Scale bars, 0.5 cm.

Additionally, the ultrasound signal became stronger when the laser power was increased to 2 W/cm<sup>2</sup> (Figure 3C). The ultrasound signal intensity of DHPL decreased to a low level immediately after “turn-off” (laser off) (Figure S5). PBS, used as a control, showed no ultrasound signal under laser exposure (Figure 3D). The results suggested that the size of DHPL increased due to the gasification of PFC under laser treatment to enhance the ultrasound signal and then switched back after irradiation (Figure 2C-E). The gray value of the region of interest (ROI), which indicates the intensity of ultrasound signal, was further analyzed by “Image J” software. As presented in Figure S6, the growing rate of DHPL was greater than H AuNS@DPL, indicating the excellent imaging property of DHPL.

### Cellular internalization

The cellular internalization of DPL, DHPL and SA-DOX was examined in MCF-7 and 4T1 cells. Large amounts of DPL, DHPL, or SA-DOX were internalized by MCF-7 cells 2 h post-incubation (Figure 4A-C). The semi-quantitative analysis of DOX fluorescence revealed that the cellular uptake behavior of SA-DOX or DPL was similar, with a maximum amount at 2 h that decreased at 6 h (Figure 4G). As for DHPL, the DOX fluorescence was significantly lower than that in the other two groups after 2 h incubation, which could be attributed to the fluorescence quenching of DOX by H AuNS. DPL, DHPL, and SA-DOX presented a similar uptake profile in 4T1 cells (Figure 4D-F, H).

### Cytotoxicity *in vitro*

Since DOX•HCl was modified to the hydrophobic SA-DOX for drug loading, its cytotoxicity had to be verified. MTT assay was employed to investigate the tumor-killing ability of SA-DOX, DOX•HCl, HPL, DPL, and DHPL. As shown in Figure 5A, in MCF-7 cells, DOX•HCl showed a much lower IC<sub>50</sub> (50 % inhibitory concentration) value (0.19 μM) compared with SA-DOX (1.06 μM). A plausible explanation of the decreased cytotoxicity might be the poor solubility of SA-DOX and the influence of the structure modification. It was gratifying that when the concentration of DOX reached 10 μM, the difference in the cell inhibition effects of SA-DOX and DOX•HCl was not statistically significant. Also, the cytotoxicity of DHPL mediated by NIR light was similar to that of DOX•HCl while DHPL without laser treatment exhibited a significantly decreased cytotoxicity. The IC<sub>50</sub> values of DHPL, DHPL plus laser and DPL were 6.20, 0.24 and 0.74 μM, respectively. It is obvious that NIR laser was able to significantly enhance the cytotoxicity of DHPL due to the heat-induced size

change and the triggered DOX release. HPL also caused cell death under NIR light due to its strong photothermal effect. Compared with MCF-7 cells, 4T1 and HEK293 cells presented better tolerance to the drugs (Figure 5B and Figure S7).

### Ultrasound imaging *in vivo*

Since the size increase of DHPL-29 was more sensitive to heat than DHPL-59 (Figure 2C-D), we chose DHPL-29 (30 μL/mL PFP; 0.5 mg/mL H AuNS) to act as the ultrasound imaging agent in 4T1 tumor-bearing mice. As displayed in Figure 6A, the ultrasound signal of tumor site became stronger under NIR light exposure (2 W/cm<sup>2</sup>) 24 h post-injection. Several microbubbles (yellow arrow) were observed in deep tumor matrix 5 min after irradiation, indicating that DHPL-29, which was accumulated in the tumor, inflated under laser treatment and exhibited enhanced ultrasound signal. After 48 h, the signal intensity increased under the same laser conditions (Figure 6B). A plausible explanation was an abundant DHPL tumor accumulation, leading to a considerably enhanced sensitivity to the temperature rise. Also, the intensity of ultrasound signal became stronger with increase in the irradiation time, demonstrating an excellent NIR light-controllable ultrasound imaging property of DHPL.

As a control, SonoVue<sup>®</sup> was also intravenously injected into the mice. Because of its large size, SonoVue<sup>®</sup> could rapidly reach the blood vessels around the tumor through blood circulation instead of penetrating them. There was no obvious ultrasound signal inside the tumor both before and after the perfusion of SonoVue<sup>®</sup>, demonstrating that SonoVue<sup>®</sup> was not suitable to be an ultrasound imaging agent for deep-tumor detection (Figure 6C).

### Biodistribution of DHPL in 4T1 tumor-bearing mice

DHPL was labeled with DiR, and the biodistribution was further investigated in 4T1 tumor-bearing balb/c mice. The fluorescence signal of DiR in the tumor was already detectable at 2 h post-injection, with a gradual increase till 48 h (Figure 7A), which could be the reason for the enhanced ultrasound signal in the tumor (Figure 6B). Large numbers of DHPL were observed in liver and spleen, probably resulting from the recognition by RES (reticular endothelial system) (Figure 7A and Figure S8). As a control, free DiR showed almost no specific accumulation in the tumors after *i.v.* injection (Figure S9). Overall, DHPL exhibited an excellent tumor accumulation facilitated by the enhanced permeability and retention (EPR) effect.



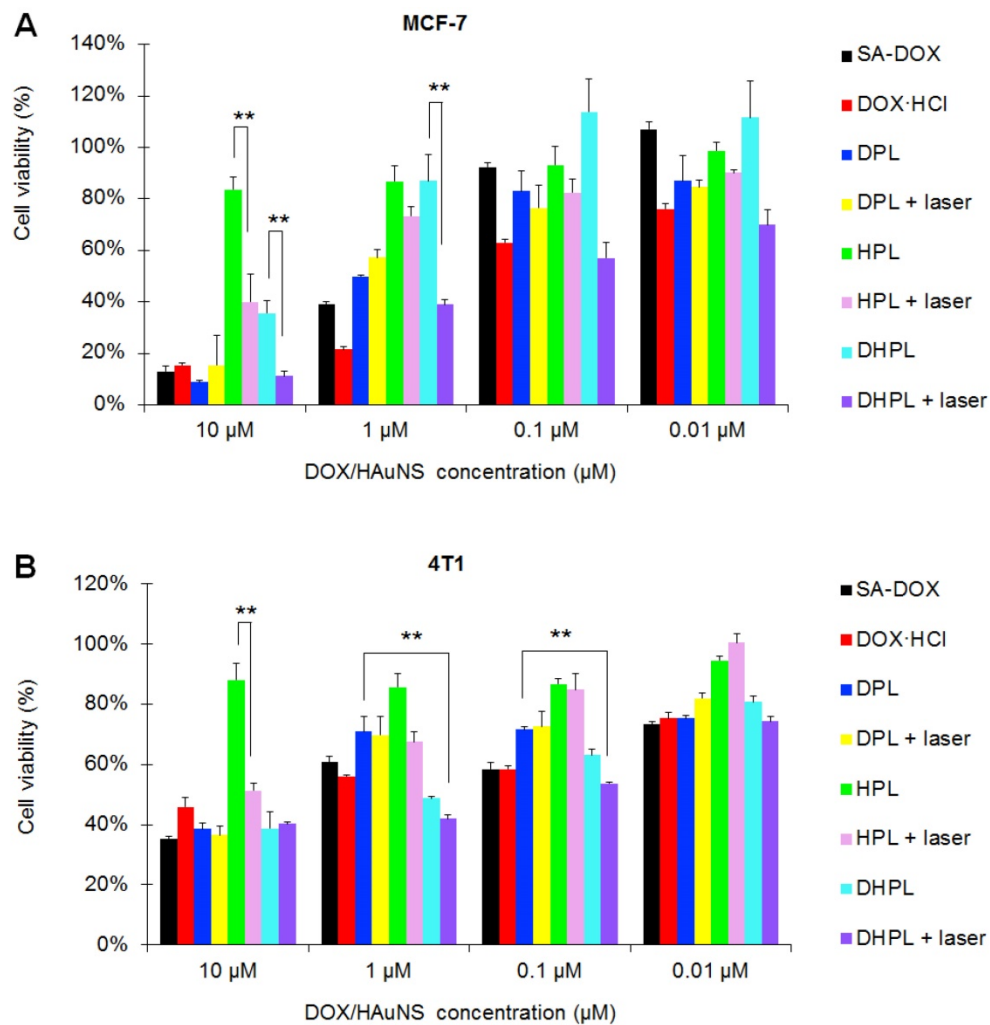


**Figure 5. Cytotoxicity.** Cell viability of MCF-7 (A) and 4T1 (B) cells treated with SA-DOX, DOX HCl, DPL, HPL, and DHPL followed by NIR light irradiation (1 W/cm<sup>2</sup>, 3 min). Cells without laser irradiation were used as controls.

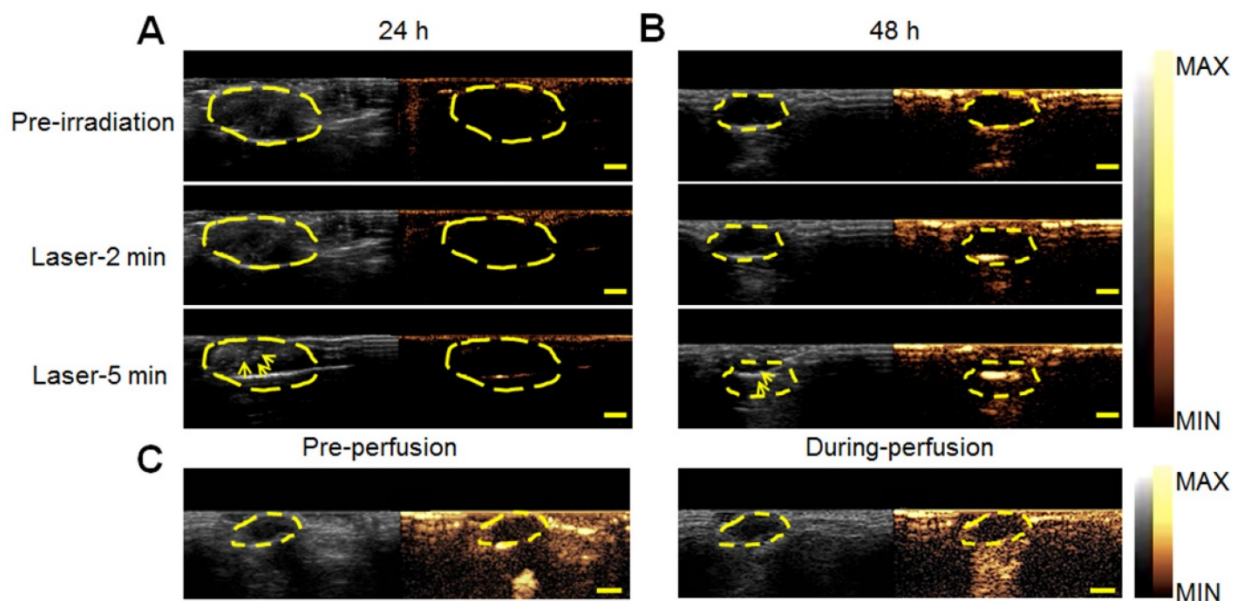


**Figure 6. Ultrasound imaging in vivo.** *In vivo* ultrasound images of tumor sites in 4T1 tumor-bearing mice at 24 h (A) or 48 h (B) post-injection of DHPL-29. The tumor sites were treated with NIR laser irradiation (2 W/cm<sup>2</sup>) for 2 min or 5 min. (C) *In vivo* ultrasound images of tumor sites in 4T1 tumor-bearing mice before and during the perfusion of SonoVue®. The yellow dotted line indicates tumor sites. The yellow arrow indicates microbubbles produced after NIR light irradiation. Scale bars, 0.5 cm.

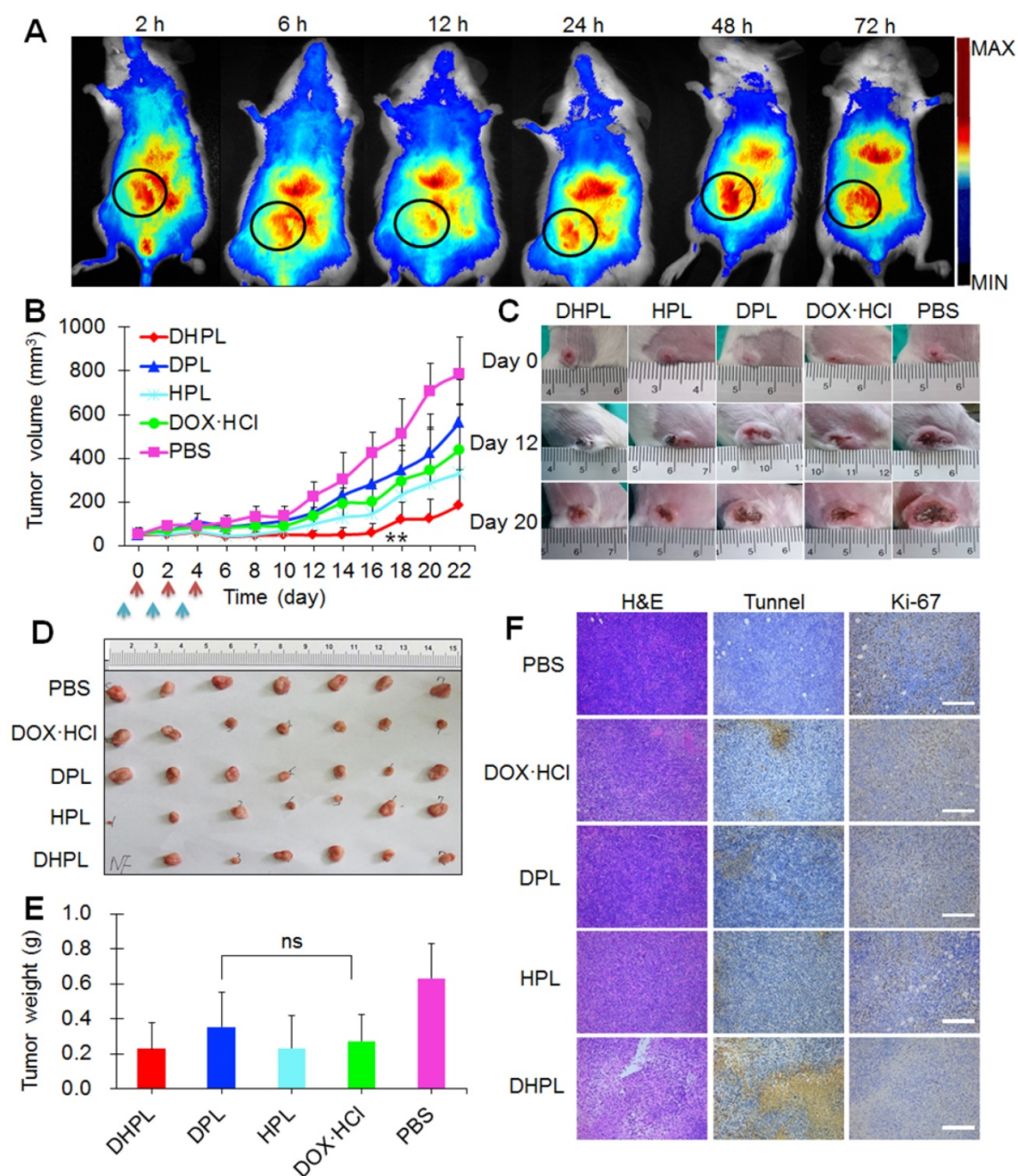


**Figure 7. Biodistribution and antitumor effect *in vivo*.** (A) Representative *in vivo* fluorescence imaging of the 4T1 tumor-bearing mice at different time point after *i.v.* injection of DiR-labeled DHPL. The black circles indicate tumors. Ex: 748 nm; Em: 780 nm. (B) The tumor growth curves for 4T1 tumor-bearing mice treated with PBS (n=7), DOX·HCl (n=7), DPL (n=7), HPL plus NIR light irradiation (1 W/cm<sup>2</sup>, 3 min, n=7) and DHPL plus NIR light irradiation (1 W/cm<sup>2</sup>, 3 min, n=7). The blue arrow indicates injections and the red arrow indicates laser irradiations. (C) Representative photographs of tumors in all groups at days 0, 12, and 20. (D) Photographs of tumors in all the groups at day 22. (E) Average tumor weights in different treatment groups. Tumors were removed on day 22. (F) The photomicrographs of H&E-stained (left), tunnel-stained (middle) and Ki-67-stained (right) tumor slides after different treatments. Scale bars, 100  $\mu$ m.

### Antitumor effect *in vivo*

Antitumor effect *in vivo* was examined in subcutaneous 4T1 tumor models. First of all, HPL or DHPL were injected intravenously into the mice to investigate their *in vivo* photothermal effect. The laser irradiation was performed 24 h post-injection and the temperature change at the tumor site was directly observed by a thermal infrared (TIR) imaging system. The temperature of tumors in HPL and DHPL group

elevated rapidly under laser exposure, reaching over 41°C within 2 min. However, tumors in the PBS group showed no obvious temperature change (Figure S10A-B). The results indicated the extraordinary light-to-heat conversion ability of HAuNS. The maximum permissible temperature of PTT *in vivo* was 40–44 °C [24]. It was clear that DHPL exhibited a great advantage due to the specific tumor accumulation and laser irradiation. The temperature of tumors

could be higher than 44° C without any damage to normal ambient tissues.

DHPL plus laser illumination exhibited the strongest tumor growth inhibition effect compared with the other four groups, especially in the first 16 days (**Figure 7B**). It was possibly due to the photothermal ablation of HAuNS and the increased SA-DOX release triggered by temperature elevation. Since there was only one drug administration cycle, two tumors in the DHPL plus laser group recurred after day 16 due to the clearance of the drugs. Representative photographs of tumors in all groups at days 0, 12, and 20 are displayed in **Figure 7C**. Tumors in the PBS group grew fastest while those in HPL plus laser (photothermal ablation alone) or DPL (chemotherapy alone) groups were slightly inhibited. However, DHPL plus laser (photothermal-chemotherapy) exhibited a significantly stronger antitumor effect. All mice were sacrificed at day 22, and their tumors were excised, photographed (**Figure 7D**), and weighed (**Figure 7E**). The average tumor weight in the DPL group was not significantly different compared with DOX•HCl group ( $p=0.142$ ), indicating that SA-DOX in DPL was able to show the same antitumor effect as DOX. The body weight of the mice in DHPL plus laser, HPL plus laser and DOX•HCl group fluctuated in the first four days (less than 10 %), suggesting that the chemotherapy from DOX•HCl or the photothermal ablation from HAuNS caused some side effect. However, the body weight recovered after the administration and kept constant until day 22 (**Figure S11A**).

H&E (used for detecting tissue damage)-, Tunnel (used for detecting cell apoptosis)-, or Ki-67 (used for detecting cell proliferation)-stained tumor slices are displayed in **Figure 7F**. It is clear that tumor cells in PBS group grew vigorously with a high proliferation rate (Ki-67 positive: brown) and no obvious cell apoptosis (Tunnel negative: blue). DOX•HCl, DPL and HPL plus laser group caused limited damage to tumor cells while DHPL plus laser group showed apparent damage to tumor tissue with large areas of cell apoptosis. The Ki-67 positive rate showed a profile of PBS > DPL > DOX•HCl > HPL plus laser > DHPL plus laser, demonstrating the strongest tumor growth inhibition effect of DHPL under laser treatment. The major tissues of mice in each group were stained by H&E for histopathology analysis. No obvious abnormality was found in all groups compared with the control PBS group (**Figure S11B**) suggesting good biocompatibility of the therapeutic procedure.

## Discussion

To combine cancer therapy with tumor

ultrasound imaging, we fabricated a dual-therapy platform employing phospholipids to co-encapsulate PFC, hydrophobic DOX (SA-DOX) and HAuNS (OMP-HAuNS). The resulting DHPL nano-system was  $196.6 \pm 17.6$  nm in size with several HAuNS inside the lipid membrane (**Figure 1B**) and exhibited an excellent light-to-heat conversion effect under NIR laser (**Figure 1C** and **Figure S4**). Because of the photothermal effect of HAuNS, the liposomes were prone to swell, thus inducing an NIR-triggered SA-DOX release (**Figure 1D**).

The phase transition of PFC from liquid to gas was responsible for increasing the size of DHPL, which was the key factor to enhance the effectiveness of ultrasound imaging. We, therefore, investigated the size changes of DHPL at different temperatures. Two kinds of PFCs (PFH, boiling point 59 °C; PFP, boiling point 29 °C) were employed for ultrasound imaging. The particle sizes of both DHPL-59 and DHPL-29 were sensitive to the temperature change (**Figure 2A-B**). Specifically, the particle size increased when temperature rose and then shrank back once the temperature was lowered (**Figure 2C-E**). Repeated steps of heating the particles were prone to weaken the extent of size enlargement, which could be attributed to the possible loss of PFC during the heating-cooling cycles. The size increase of DHPL-29 under laser irradiation was greater than that of DHPL-59 due to the lower boiling point of PFP. In general, DHPL was able to serve as an ideal ultrasound imaging agent controlled by NIR light both *in vitro* (**Figure 3**) and *in vivo* (**Figure 6**).

The cellular internalization of DPL, DHPL, and SA-DOX in MCF-7 and 4T1 cells was examined. Overall, the uptake of the drugs by these two different cell lines appeared to be fast, with immense DOX fluorescence within 2 hours (**Figure 4A-F**). SA-DOX was capable of entering into the nucleus. The cellular uptake of DPL was similar to that of SA-DOX, which reached a peak at 2 h, decreased at 6 h, and then increased again at 12 h (**Figure 4G-H**). A plausible explanation for the quick release of SA-DOX could be because of PFC. As for DHPL, the lower DOX fluorescence at 2 h could be attributed to the fluorescence quenching of DOX by HAuNS. After releasing from DHPL, the fluorescence of SA-DOX at later time points could recover.

Due to the efficient cellular internalization and the combined effect of photothermal ablation and chemotherapy, DHPL plus laser illumination exhibited obvious cytotoxicity to both MCF-7 and 4T1 tumor cells (**Figure 5**). Furthermore, DHPL showed considerable accumulation into tumors after intravenous injection (**Figure 7A** and **Figure S8**). Consequently, DHPL exhibited the strongest 4T1

tumor growth inhibition mediated by 808 nm NIR light irradiation (**Figure 7B**). Tumors in this group were severely damaged (**Figure 7F**). Major tissues in all treatment groups appeared normal which was comparable to the control PBS group, indicating the safety of the therapeutic method (**Figure S11B**).

## Conclusion

In this study, we fabricated an NIR light-triggered multifunctional PFC liposome for ultrasound imaging and tumor therapy. DOX and HAuNS were co-encapsulated in the liposomes to realize the photothermal combined chemotherapy. The constructed DHPL exhibited a homogeneous size distribution around 200 nm and an extraordinary photothermal effect under 808 nm NIR laser irradiation. Furthermore, the heat produced by HAuNS was sufficient for triggering SA-DOX release, PFC gasification, and controlling the size conversion of DHPL. Thus, DHPL was an excellent ultrasound imaging agent both *in vitro* and *in vivo*. Due to its efficient internalization by MCF-7 and 4T1 cells, DHPL exerted a dramatically enhanced cytotoxicity when exposed to laser treatment. Compared with the conventional ultrasound imaging agents (microbubbles), DHPL showed considerable accumulation at the tumor sites due to its nanometer size. It also imparted an enhanced ultrasound signal in deep tumor tissue due to the significantly increased size under light irradiation. Because of the combined photothermal ablation and chemotherapy, DHPL also exhibited increased tumor growth inhibitory effect compared with photothermal therapy or chemotherapy alone. In conclusion, our study revealed that DHPL, with NIR light irradiation, can serve as a potentially effective ultrasound imaging-guided, photothermal/chemo cancer therapy system.

## Abbreviations

DHPL: doxorubicin and hollow gold nanospheres loaded PFC liposome; DLS: dynamic light scattering; DMEM: Dulbecco's Modified Eagle Medium; DOX: doxorubicin; DPL: doxorubicin loaded PFC liposome; DSPE-PEG<sub>2000</sub>: 1,2-distearoyl-sn-glycero-3-phosphoethanolamine-N-[methoxy(polyethylene-glycol)-2000]; EDC: Ethyl-3-(3-dimethylaminopropyl) carbodiimide; FBS: fetal bovine serum; HAuNS: hollow gold nanospheres; HPL: hollow gold nanospheres loaded PFC liposome; HPMC: hydroxy-propyl methyl cellulose; MTT: 3-(4,5-dimethylthiazol-2-yl)-2,5-diphenyltetrazolium bromide; NIR: near-infrared; OMP: octadecyl 3-mercaptopionate; PFC: perfluorocarbon; PFH: perfluorohexane; PFP: perfluoropentane; PTT:

photothermal therapy; RPMI: RPMI-1640 medium; SA: stearic acid; TEM: transmission electron microscope.

## Supplementary Material

Supplementary figures.

<http://www.thno.org/v08p3059s1.pdf>

## Acknowledgments

This work was funded by the National Natural Science Foundation of China (81373348 and 81573365). It was also supported by the National Natural Science Foundation of China (81471664).

## Competing Interests

The authors have declared that no competing interest exists.

## References

- Selbekk T, Jakola AS, Solheim O, Johansen TF, Lindseth F, Reinertsen J, et al. Ultrasound imaging in neurosurgery: approaches to minimize surgically induced image artefacts for improved resection control. *Acta Neurochir.* 2013; 155: 973-80.
- Gramiak R, Shah PM. Echocardiography of the aortic root. *Invest Radiol.* 1968; 3: 356-66.
- Koh J, Jung DC, Oh YT, Yoo MG, Noh S, Han KH, et al. Additional targeted biopsy in clinically suspected prostate cancer: prospective randomized comparison between contrast-enhanced ultrasound and sonoelastography guidance. *Ultrasound Med Biol.* 2015; 41: 2836-41.
- Hudson JM, Williams R, Tremblay-Darveau C, Sheeran PS, Milot L, Bjarnason GA, et al. Dynamic contrast enhanced ultrasound for therapy monitoring. *Eur J Radiol.* 2015; 84: 1650-1657.
- Moon H, Kang J, Sim C, Kim J, Lee H, Chang JH, et al. Multifunctional theranostic contrast agent for photoacoustics- and ultrasound-based tumor diagnosis and ultrasound-stimulated local tumor therapy. *J Control Release.* 2015; 218: 63-71.
- Li F, Bai M, Wu Y, He Y, Gu J, Xing J, et al. Comparative diagnostic performance of contrast-enhanced ultrasound versus baseline ultrasound for renal pelvis lesions. *Ultrasound Med Biol.* 2015; 41: 3109-19.
- Durkin N, Deganello A, Sellars ME, Sidhu PS, Davenport M, Makin E. Post-traumatic liver and splenic pseudoaneurysms in children: Diagnosis, management, and follow-up screening using contrast enhanced ultrasound (CEUS). *J Pediatr Surg.* 2016; 51: 289-92.
- Chen J, Ratnayaka S, Alford A, Kozlovskaya V, Liu F, Xue B et al. Theranostic multilayer capsules for ultrasound imaging and guided drug delivery. *ACS Nano.* 2017; 11: 3135-46.
- Wang Z, Qiao R, Tang N, Lu Z, Wang H, Zhang Z, et al. Active targeting theranostic iron oxide nanoparticles for MRI and magnetic resonance-guided focused ultrasound ablation of lung cancer. *Biomaterials.* 2017; 127: 25-35.
- Shiraiishi K, Endoh R, Furuhashi H, Nishihara M, Suzuki R, Maruyama K, et al. A facile preparation method of a PFC-containing nano-sized emulsion for theranostics of solid tumors. *Int J Pharm.* 2011; 421: 379-87.
- Wheatley MA, Forsberg F, Dube N, Patel M, Oeffinger BE. Surfactant-stabilized contrast agent on the nanoscale for diagnostic ultrasound imaging. *Ultrasound Med Biol.* 2006; 32: 83-93.
- Wang D, Yang K, Gao YH, Tan KB, Liu Z. Preparation and characterization of a nanoscale ultrasound contrast agent. *Clin Imaging.* 2010; 34: 288-92.
- Wust P, Hildebrandt B, Sreenivasa G, Rau B, Gellermann J, Riess H, et al. Hyperthermia in combined treatment of cancer. *Lancet Oncol.* 2002; 3: 487-97.
- Schneider CC, Archid R, Fischer N, Bühler S, Venturini S, Berger A, et al. Metabolic alteration—overcoming therapy resistance in gastric cancer via PKG-1 inhibition in a combined therapy with standard chemotherapeutics. *Int J Surg.* 2015; 22: 92-8.
- Diez B, Ernst G, Teijo MJ, Battle A, Hajos S, Fukuda H. Combined chemotherapy and ALA-based photodynamic therapy in leukemic murine cells. *Leuk Res.* 2012; 36: 1179-84.
- Wang H, Zhao R, Li Y, Liu H, Li F, Zhao Y, et al. Aspect ratios of gold nanoshell capsules mediated melanoma ablation by synergistic photothermal therapy and chemotherapy. *Nanomedicine.* 2016; 12: 439-48.
- Coughlin AJ, Ananta JS, Deng N, Larina IV, Decuzzi P, West JL. Gadolinium-conjugated gold nanoshells for multimodal diagnostic imaging and photothermal cancer therapy. *Small.* 2014; 10: 556-65.
- Li W, Zhang H, Guo X, Wang Z, Kong F, Luo L. Gold nanospheres-stabilized indocyanine green as a synchronous photodynamic-photothermal therapy

- platform that inhibits tumor growth and metastasis. *ACS Appl Mater Interfaces*. 2017; 9: 3354-67.
- [19] Yuan H, Khoury CG, Wilson CM, Grant GA, Bennett AJ, Vo-Dinh T. In vivo particle tracking and photothermal ablation using plasmon-resonant gold nanostars. *Nanomedicine*. 2012; 8: 1355-63.
- [20] Arunkumar P, Raju B, Vasantharaja R, Vijayaraghavan S, Preetham Kumar B, Jeganathan K, Premkumar K, et al. Near infra-red laser mediated photothermal and antitumor efficacy of doxorubicin conjugated gold nanorods with reduced cardiotoxicity in swiss albino mice. *Nanomedicine*. 2015; 11: 1435-44.
- [21] Bao T, Yin W, Zheng X, Zhang X, Yu J, Dong X, et al. One-pot synthesis of PEGylated plasmonic MoO(3-x) hollow nanospheres for photoacoustic imaging guided chemo-photothermal combinational therapy of cancer. *Biomaterials*. 2016; 76: 11-24.
- [22] Li W, Guo X, Kong F, Zhang H, Luo L, Li Q, et al. Overcoming photodynamic resistance and tumor targeting dual-therapy mediated by indocyanine green conjugated gold nanospheres. *J Control Release*. 2017; 258: 171-81.
- [23] Liu X, Li B, Fu F, Xu K, Zou R, Wang Q, et al. Facile synthesis of biocompatible cysteine-coated CuS nanoparticles with high photothermal conversion efficiency for cancer therapy. *Dalton Trans*. 2014; 43: 11709-15.
- [24] Hwang S, Nam J, Jung S, Song J, Doh H, Kim S. Gold nanoparticle-mediated photothermal therapy: current status and future perspective. *Nanomedicine*. 2014; 9: 2003-22.